

## Experimental assessment of the piezoelectric transverse $d_{15}$ shear sensing mechanism

Pelin Berik<sup>1a</sup>, Ayech Benjeddou<sup>\*2</sup> and Michael Krommer<sup>1b</sup>

<sup>1</sup>Institute for Technical Mechanics, Johannes Kepler University, 4040 Linz, Austria

<sup>2</sup>Structures, Institut Supérieur de Mécanique de Paris, 93400 Saint Ouen, France

(Received November 8, 2013, Revised January 20, 2014, Accepted January 24, 2014)

**Abstract.** The piezoelectric transverse  $d_{15}$  shear sensing mechanism is firstly assessed experimentally for a cantilever smart sandwich plate made of a piezoceramic axially poled patched core and glass fiber reinforced polymer composite faces. Different electrical connections are tested for the assessment of the sensor performance under a varying amplitude harmonic (at 24 Hz) force. Also, the dynamic response of the smart sandwich composite structure is monitored using different acquisition devices. The obtained experimentally sensed voltages are compared to those resulting from the benchmark three-dimensional piezoelectric coupled finite element simulations using a commercial code where realistic features, like equipotential conditions on the patches' electrodes and mechanical updating of the clamp, are considered. Numerically, it is found that the stiffness of the clamp, which is much softer than the ideal one, has an enormous influence on the sensed voltage of its adjacent patch; therefore, sensing with the patch on the free side would be more advantageous for a cantilever configuration. Apart from confirming the latter result, the plate benchmark experimental assessment showed that the parallel connection of its two oppositely poled patches has a moderate performance but better than the clamp side patch acting as an individual sensor.

**Keywords:** piezoceramic  $d_{15}$  shear sensing; piezoelectric composite sandwich plate; harmonic sensing experiments; finite element simulations; mechanical updating; electrical connections

### 1. Introduction

Smart structures and systems need sensors for measuring a variety of outputs like displacements, strains and forces (or pressures). For this purpose, piezoelectric materials are the most used *dynamic active* strain sensors. Depending on its material initial polarization and electrodes configuration, a piezoelectric sensor can measure a *longitudinal strain* thanks to the *longitudinal* piezoelectric response mode that uses the *longitudinal* piezoelectric strain coupling constant  $d_{33}$  (Han and Shi 2012), *in-plane strains* thanks to the *transverse* piezoelectric response mode that uses the *transverse* piezoelectric strain coupling constant  $d_{31}$  (Rausch *et al.* 2012), and *shear strains* thanks to the *shear* response mode that uses the *shear* piezoelectric coupling constant  $d_{15}$  (Benjeddou 2007).

---

\*Corresponding author, Professor, E-mail: benjeddou@supmeca.fr

<sup>a</sup> Dr., researcher

<sup>b</sup> Associate Professor

Two types of piezoelectric materials are commonly used for dynamic active strain sensing: piezoelectric *polymers*, which popular representative is *polyvinylidene difluoride* (PVDF), and piezoelectric *ceramics* (shortly piezoceramics), which popular representative is the *lead zirconate titanate* (PZT). Fundamentally, *PZT sensors* are suited for measurement of the *longitudinal strain*, when used in powder (distributed in a cement or polymer matrix) or fiber (generally reinforcing a polymer matrix) forms, and of the *shear strain*, when used in tubular or plate (disc or rectangular) forms, while *PVDF sensors* are mainly suitable for *in-plane normal strains* measurements since it is often used in a film form. It is worth to recall that *PVDFs* have very poor (almost nil) shear piezoelectric coupling constants; hence, they are not suited for *direct* shear strain sensing. However, it was proved recently (Ma *et al.* 2012) that, when arranged in a special rosette configuration, the in-plane shear strain can be measured *indirectly*; i.e., through  $d_{31}$  and  $d_{33}$  constants but not  $d_{15}$  one.

In order to avoid the well-known *drift* (decay of charge) phenomena of the output signal with time (Van Den Ende *et al.* 2010), piezoelectric-induced strain sensing is often conducted under *quasi-static* (at minimum frequency  $f_{\min} \geq 0.5$  Hz) conditions (Kursu *et al.* 2009, Melnykowycz and Brunner 2011, Konca and Wahab 2012); generally, the small generated amount of charge that drains through the resistances of the measurement circuit can be reduced through the use of a charge amplifier (Chevallier *et al.* 2013). Alternatively, defining a bandwidth higher (or equal) than 20Hz and using an instrumentation amplifier with a high input impedance is sufficient to fulfill this dynamic requirement (Rausch *et al.* 2012). This alternative approach was retained here for the present dynamic sensing experiments. For this purpose, a frequency of 24 Hz, which is well below the investigated smart plate first mode, was retained for the applied varying amplitude harmonic force.

Compared to longitudinal and transverse strain sensing, shear strain sensing is much less investigated; in particular experimentally. Indeed, in the last available survey on piezoelectric shear actuation and sensing (Benjeddou 2007), only a technical note was found on  $d_{15}$  shear-induced *torsion* sensing using a *tubular* piezoceramic device (Sung *et al.* 1994). Since then, it is only recently that shear strains have been measured under a torsion torque excitation and using a shear piezoceramic core made of sixteen piezoceramic *rectangular* patches arranged in two length-wise oppositely poled (OP) rows and sandwiched between two glass fiber reinforced polymer (GFRP) matrix-based composite faces (Chevallier *et al.* 2013). This benchmark was initially developed for shear-induced direct torsion actuation (Berik *et al.* 2013); hence, the used measurement concept relies on the *torsion sensing mechanism* (TSM). Therefore, from the current state of art, it can be noticed that the *direct* piezoelectric *shear sensing mechanism* (SSM) has not yet been experimented. It is then the objective of the present contribution to fill this gap.

Therefore, for the purpose of SSM experimental assessment, an axially OP  $d_{15}$  shear strain sensing configuration that is adapted from the shear actuation benchmarks proposed in Berik and Benjeddou (2011) is here designed, experimented and simulated using three-dimensional (3D) coupled piezoelectric finite elements (FE) within the general purpose FE software ABAQUS®. That is, the investigated structural benchmark is a cantilever sandwich *plate* made of *two in-ward* OP length-wise patched shear piezoceramic core and GFRP faces. It is worth to notice that, in contrary to the usual *out-ward* OP patched configurations that were designed for piezoelectric micro-pumping (Cheng *et al.* 2005, Benjeddou *et al.* 2006) and piezoelectric energy harvesting (Wang and Liu 2011) applications, the in-ward OP configuration proposed in this paper has no non-electroded region between the length-wise OP patches.

Hereafter, the piezoelectric  $d_{15}$  shear sensing mechanism is first recalled; then, the proposed sandwich smart *plate* benchmark setup design, dynamic (harmonic at 24 Hz) sensing experiments and corresponding FE simulations are presented. Finally, some conclusions are given as a closure.

### 2. Piezoelectric $d_{15}$ shear sensing mechanism

The sensing functionality of a *piezoceramic* material is governed by its *direct* piezoelectric effect. Written in the *d-form*, the corresponding 3D constitutive equation relates the electric displacements to the mechanical stresses and electric fields. Hence, when the convention that the material initial poling direction should be along the material *third* axis is retained, the constitutive relation

$$\begin{Bmatrix} D_1 \\ D_2 \\ D_3 \end{Bmatrix} = \begin{bmatrix} 0 & 0 & 0 & 0 & d_{15} & 0 \\ 0 & 0 & 0 & d_{15} & 0 & 0 \\ d_{31} & d_{31} & d_{33} & 0 & 0 & 0 \end{bmatrix} \begin{Bmatrix} T_1 \\ T_2 \\ T_3 \\ T_4 \\ T_5 \\ T_6 \end{Bmatrix} + \begin{bmatrix} \epsilon_{11}^T & 0 & 0 \\ 0 & \epsilon_{11}^T & 0 \\ 0 & 0 & \epsilon_{33}^T \end{bmatrix} \begin{Bmatrix} E_1 \\ E_2 \\ E_3 \end{Bmatrix} \quad (1)$$

holds. Here,  $T_p, D_i, E_k$  ( $p = 1, \dots, 6; i, k = 1, 2, 3$ ) are the stresses, electric displacements and electric fields;  $d_{ip}, \epsilon_{ik}^T$  are the *strain* piezoelectric coupling and *free* (at constant stress) dielectric constants.

The shear piezoelectric response can be activated when the induced electric field and the poling directions are *perpendicular*; besides, in practice, the piezoceramic material is generally coated with conducting *electrodes* for the measurement of the sensing signal. Hence, for a piezoceramic patch that is poled along its *third* material axis and electroded on its major surfaces, as in Fig. 1(a), this leads to a dominant thickness component of the electric field ( $E_1$ ) so that Eq. (1) reduces to

$$\begin{Bmatrix} D_1 \\ D_2 \\ D_3 \end{Bmatrix} = \begin{bmatrix} 0 & 0 & 0 & 0 & d_{15} & 0 \\ 0 & 0 & 0 & d_{15} & 0 & 0 \\ d_{31} & d_{31} & d_{33} & 0 & 0 & 0 \end{bmatrix} \begin{Bmatrix} T_1 \\ T_2 \\ T_3 \\ T_4 \\ T_5 \\ T_6 \end{Bmatrix} + \begin{bmatrix} \epsilon_{11}^T & 0 & 0 \\ 0 & \epsilon_{11}^T & 0 \\ 0 & 0 & \epsilon_{33}^T \end{bmatrix} \begin{Bmatrix} E_1 \\ 0 \\ 0 \end{Bmatrix} \quad (2)$$

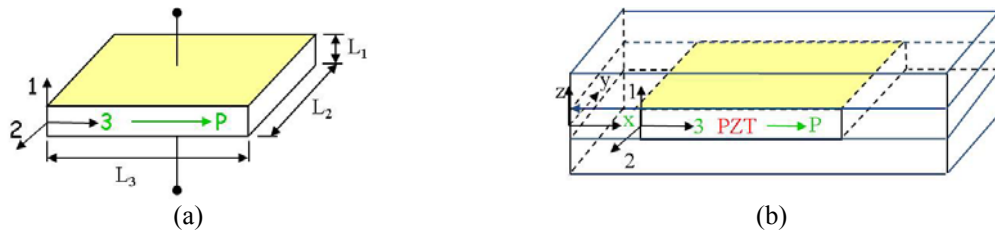


Fig. 1 Individual (a) and sandwiched (b) piezoceramic  $d_{15}$  shear patch electroded on its major surfaces

Hence, for the case the electrodes of the patch are *short-circuited* (SC) (using a charge amplifier for example), the dominant component of the electric field can be considered as nil, so that Eq. (2) further reduces to

$$\begin{Bmatrix} D_1 \\ D_2 \\ D_3 \end{Bmatrix} = \begin{bmatrix} 0 & 0 & 0 & | & 0 & d_{15} & 0 \\ 0 & 0 & 0 & | & d_{15} & 0 & 0 \\ d_{31} & d_{31} & d_{33} & | & 0 & 0 & 0 \end{bmatrix} \begin{Bmatrix} T_1 \\ T_2 \\ T_3 \\ T_4 \\ T_5 \\ T_6 \end{Bmatrix} \quad (3)$$

Nevertheless, for the electroded patch as in Fig. 1(a), the SC sensor electric charge at the bottom electrode can be computed only from the *thickness* electric displacement component ( $D_1$ ) using the relation

$$Q_{SC} = \int_{A_e} \vec{D} \cdot \vec{n} \, dA = \int_{A_e} \vec{D} \cdot \vec{e}_1 \, dA = \int_{A_e} D_1 \, dA \quad (4)$$

where an arrow indicates a vector quantity,  $\vec{n}$  ( $\vec{e}_1$ ) is the unit vector in thickness direction,  $A_e$  denotes the two electrodes area, and the thickness component of the electric displacement  $D_1$  is computed from Eq. (3) as

$$D_1 = d_{15} T_5 \quad (5)$$

It can then be concluded from Eq. (5) that, regardless of the loading stress components number, the *normal* electric displacement  $D_1$  couples only with the transverse *shear* stress  $T_5$  through the *shear* strain piezoelectric coupling constant  $d_{15}$ ; this motivates the  $d_{15}$  *shear sensing mechanism* denomination. The SSM is then independent from any other ( $d_{31}$  or  $d_{33}$ ) piezoelectric response; it is also related to the  $x_3$ - $x_1$  *transverse* plane only. As can be seen from Eq. (5) also, the shear sensing occurs only under a loading shear stress state. This can be reached by *sandwiching* the patch shear sensor between stiff elastic skins as sketched in Fig. 1(b) for example. In this case, since the poling direction, indicated in Fig. 1(b) by the horizontal arrow followed by the letter P, lies along the *global* first ( $x$ ) axis, Eq. (3) in the global coordinate system ( $x, y, z$ ) can be written as

$$\begin{Bmatrix} D_x \\ D_y \\ D_z \end{Bmatrix} = \begin{bmatrix} \bar{d}_{11} & \bar{d}_{12} & \bar{d}_{13} & | & 0 & 0 & 0 \\ 0 & 0 & 0 & | & 0 & 0 & \bar{d}_{26} \\ 0 & 0 & 0 & | & 0 & \bar{d}_{35} & 0 \end{bmatrix} \begin{Bmatrix} \sigma_{xx} \\ \sigma_{yy} \\ \sigma_{zz} \\ \tau_{yz} \\ \tau_{xz} \\ \tau_{xy} \end{Bmatrix} \quad (6)$$

Here  $\sigma_{ii}$ ,  $i = x, y, z$ , denotes the normal stresses and  $\tau_{ij}$ ,  $j \neq i$ , and  $i, j = x, y, z$ , the shear ones; a *bar* has been used for denoting the *global* strain piezoelectric coupling constants.

Due to the rotational nature of the local-to-global coordinate system transformation, the global strain piezoelectric coupling constants of Eq. (6) can be linked to the local ones via these relations

$$\bar{d}_{11} = d_{33}, \bar{d}_{12} = d_{31}, \bar{d}_{13} = d_{31}, \bar{d}_{26} = d_{15}, \bar{d}_{35} = d_{15} \quad (7)$$

Substituting Eq. (7) into Eq. (6) transforms the global expression of the thickness component of the electric displacement, see Eq. (5), to

$$D_z = d_{15} \tau_{xz} \quad (8)$$

Using this relation back in Eq. (4) provides the following expression of the collected electric charges on the electrodes of the shear piezoceramic sensor

$$Q_{SC} = \frac{1}{2} \left( \int_{A_e^-} d_{15} \tau_{xz}(x, y, z = -\frac{h_p}{2}) dx dy + \int_{A_e^+} d_{15} \tau_{xz}(x, y, z = \frac{h_p}{2}) dx dy \right) \quad (9)$$

Here, we compute half the sum of the total charge at the bottom electrode and the negative total charge at the top electrode, in order to eliminate possible deviations of these entities, which may result from the mechanical assumptions for the shear stress; e.g. it might not be constant through the thickness of the patch.  $h_p$  denotes the thickness of the piezoceramic sensor and +/- indicates top/bottom electrodes.

It can then be concluded from Eq. (9) that, in the configuration of Fig. 1(b), the more the sandwich interfaces are sheared the higher the produced electrical charges are; hence, the better is the sensing signal. Therefore, under a bending loading, the interface shear stresses are mainly due to the relative deformations (displacements) of the faces against the core shear sensor.

For illustration, consider the first-order shear deformation theory (FSDT), which assumes *through-the-thickness constant* transverse shear strain ( $\gamma_{xz}$ ), stress ( $\tau_{xz}$ ) and deflection (thickness displacement,  $w$ ); therefore, having in mind the FSDT kinematics and the shear stress-shear strain linear relation via the shear modulus  $G_{xz}$ , the elastic shear constitutive equation can be written as

$$\tau_{xz} = G_{xz} \gamma_{xz} = G_{xz} \left( \beta_x + \frac{\partial w}{\partial x} \right) \quad (10)$$

where  $\beta_x$  is the cross-section bending rotation. Moreover, we have used the fact that the axial component of the electric field is negligible; otherwise, it would be present in Eq. (10).

Using again the previous constitutive relation in the electric charge, Eq. (9), leads to the total charge for the short-circuited conditions

$$Q_{SC} = d_{15} G_{xz} \int_{A_p} \beta_x(x, y) dx dy + d_{15} G_{xz} \int_{A_p} \frac{\partial w}{\partial x}(x, y) dx dy \quad (11)$$

Where  $A_p = B_p \times L_p$  is the area of one of the two identical electrodes of the piezoceramic patch;  $B_p$  and  $L_p$  are the corresponding width and length.

After integrating the second term of Eq. (11) along the  $x$ -direction, the collected amount of shear sensing-induced electric charge can be expressed as

$$Q_{SC} = d_{15} G_{xz} \int_{A_p} \beta_x(x, y) dx dy + d_{15} G_{xz} \int_0^{B_p} [w(L_p, y) - w(0, y)] dy \quad (12)$$

It can be concluded from the previous equation that the cross-section bending rotation – induced electric charge (first term of Eq. (12)) and the one from the deflection should add positively in order to get a performant sensing signal. However, addition of opposite sign terms of

Eq. (12) would weaken or even cancel the sensing signal. Hence, the shear-induced from bending is critically governed by the patch bending rotation and its *width (y)-dependent x-edges* relative deflections.

It is worth to mention that if the shear stress is uniform on the patch electrodes, the SC sensor collected electric charge can be written from Eq. (8) as

$$Q_{SC} = d_{15} A_p \tau_{xz} \quad (13)$$

For the case the electrodes of the patch are left open (open-circuit or OC conditions; using a voltage amplifier for example), the dominant electric displacement component  $D_1$  can be considered nil so that the dual electric field component  $E_1$  can be written, from the electric field – potential ( $\varphi$ ) relation and Eq. (2) first line, as

$$E_1 = -\frac{\partial \varphi}{\partial z} = -\frac{1}{\epsilon_{11}^T} d_{15} T_5 \quad (14)$$

The SC electric potential can then be obtained from through-the-thickness integration of Eq. (14) leading to a through-the-thickness constant voltage expression, when the shear stress is constant through-the-thickness as in the FSDT framework

$$V_{OC} = \frac{h_p}{\epsilon_{11}^T} d_{15} T_5 \quad (15)$$

Now introducing the patch electric *free* capacitance,  $C_p^T = \frac{A_p \epsilon_{11}^T}{h_p}$ , in Eq. (15) transforms it to

$$V_{OC} = \frac{d_{15}}{C_p^T} A_p T_5 \quad (16)$$

It can be then expected from Eqs. (13) and (16) that, independently of the electric condition, the sensed voltage should have a linear relationship with the applied shear stress or shear resultant force  $F_3 = A_p T_5$  (or  $F_x = A_p \tau_{xz}$ ) if the applied (or bending induced) shear stress is uniform on the electrodes area.

In a general situation, for which the electrodes are neither short-circuited nor left open, a transducer equation relating the electrodes charge  $Q$  and the electric potential  $V$  can be derived as follows. We start with Eq. (1) and assume that the charge equation of electrostatics reduces to a one-dimensional form; hence, to  $D_{1,1} = 0$ , from which we conclude that  $D_1$  is constant through the patch thickness. Therefore, one can integrate over the thickness and divide by the thickness of the piezoelectric patch  $h_p$ .

$$D_1 = \frac{1}{h_p} \int_{-h_p/2}^{h_p/2} D_1 dz = \frac{1}{h_p} \int_{-h_p/2}^{h_p/2} \epsilon_{11}^T E_1 dz + \frac{1}{h_p} \int_{-h_p/2}^{h_p/2} d_{15} T_5 dz \quad (17)$$

The first integral results into the electric potential  $V$ , which is defined as the line integral over the tangential component of the electric field vector; in our case the component  $E_1$ . The charge at the electrodes is then defined as the hull integral over an electrode, from which we derive the

transducer equation

$$Q = \left( \frac{\epsilon_{11}^T}{h_p} A_e \right) V + \frac{1}{h_p} \int_{A_e} \left( \int_{-h_p/2}^{h_p/2} d_{15} T_5 dz \right) dA = C_P^T V + \frac{1}{h_p} \int_{A_e} \left( \int_{-h_p/2}^{h_p/2} d_{15} T_5 dz \right) dA \quad (18)$$

Eq. (9) for the short-circuit condition,  $V = 0$ , is obtained for the case the shear stress  $T_5$  is constant through the thickness. Eq. (15) for the open-circuit condition with  $Q = 0$  follows with a through-the-thickness and electrodes area-wise constant shear stress  $T_5$ . In general, Eq. (18) is valid also for non constant  $T_5$ ; both, with respect to the thickness as well as with respect to the electrodes area.

### 3. Smart sandwich plate benchmark investigations

The SSM is here firstly investigated for a cantilever piezoceramic smart sandwich *plate* benchmark; the latter is described in the subsequent sub-section. Then, the SSM experimental assessment is detailed. Finally, the tests numerical verifications are reached through the benchmark 3D piezoelectric coupled FE simulations using the general purpose FE code ABAQUS®.

#### 3.1 Benchmark description and tests

The smart sandwich plate benchmark is shown in Fig. 2(a); it is designed and assembled using two  $d_{15}$  shear PZT PIC255 patches (from PI Germany) of dimensions  $25 \times 25 \times 0.5 \text{ mm}^3$  sandwiched adhesively between two elastic GFRP composite faces. The latter are made of Polyspeed G-EW 760R glass fiber/epoxy layers (from Hexcel Austria) with dimensions of  $50 \times 25 \times 0.5 \text{ mm}^3$ . The piezoceramic patches are glued on their major surfaces (without vertical inter-patch bonding) in an *in-ward* OP configuration with a *non-conductive* adhesive (Henkel Loctite 9466).

The dynamic sensing experiments are carried out on the experimental benchmark shown in Fig. 3 by applying a dynamic (AC) force to the middle of the smart sandwich plate free edge using a shaker and by sensing the maximum produced voltage from the OP piezoceramic shear core according to a given electric connection of the patches.

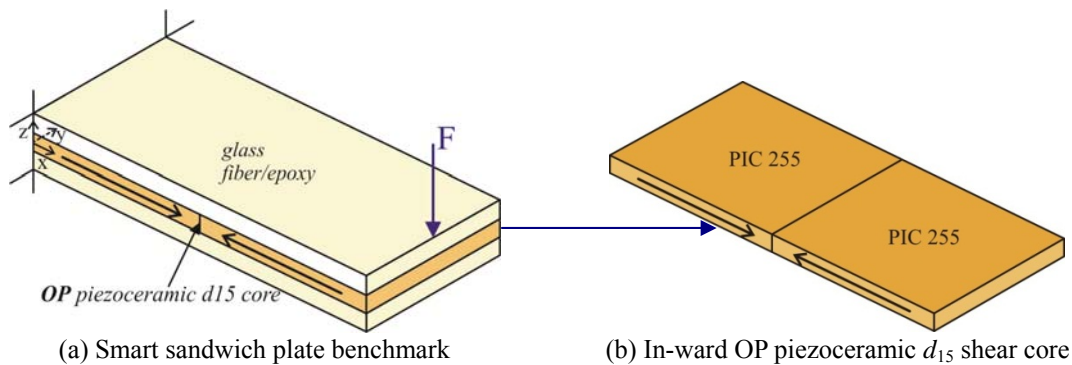


Fig. 2 Smart sandwich plate benchmark and its in-ward OP piezoceramic  $d_{15}$  shear

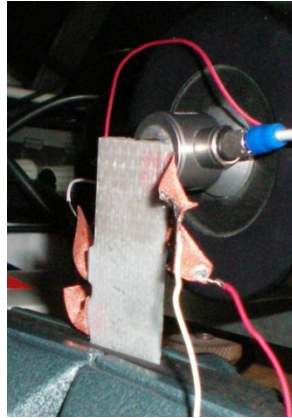
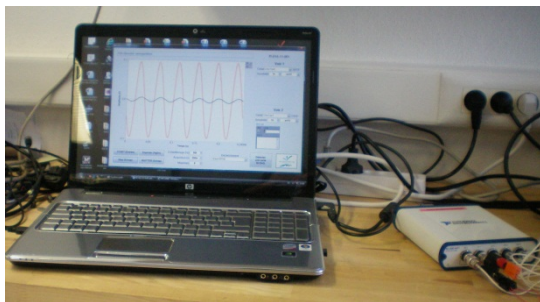
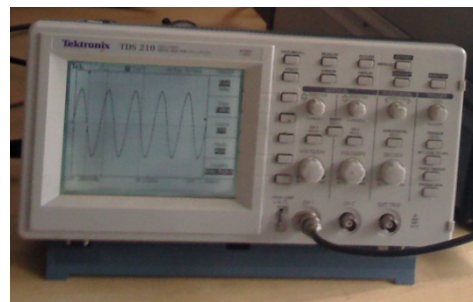


Fig. 3 Experimental cantilever smart sandwich plate setup



(a) PC and acquisition board



(b) Digital oscilloscope



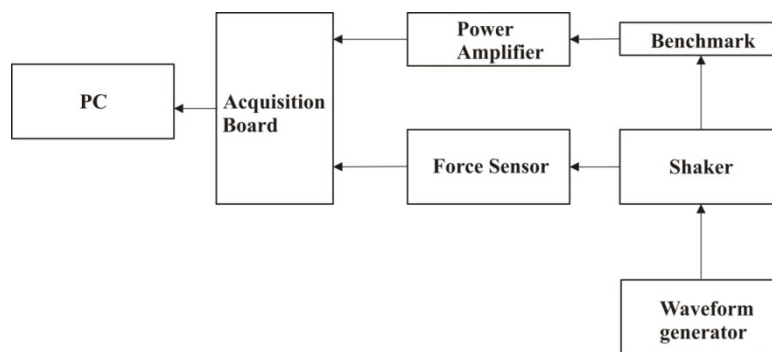
(c) Wave generator (top) and power amplifier (bottom)

Fig. 4 Measurement equipments used for the smart sandwich plate  $d_{15}$  shear sensing experiments

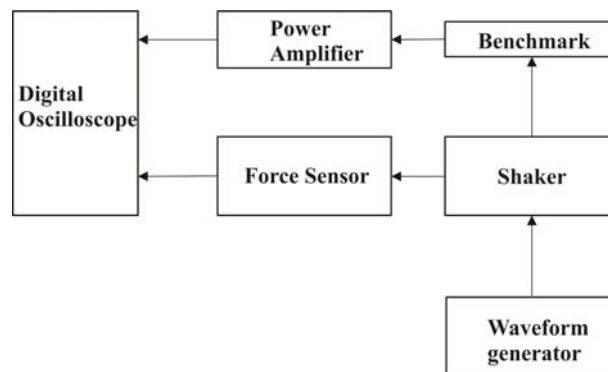
The dynamic (at 24 Hz well below the cantilever smart plate first mode, which is around 268 Hz) force amplitudes range from 0.35 to 2.8 N for the measurements using an acquisition board (NI USB-4431) via a PC, shown in Fig. 4(a), and from 0.34 to 2.67 N for the measurements using an oscilloscope (Tektronix TDS 210), shown in Fig. 4(b). The latter measurement device has a resistance of 1 M $\Omega$  in parallel with a capacitance of 20 pF, whereas the former device has a resistance of only 200 k $\Omega$  in parallel with a capacitance of 130 pF. Compared to an infinite resistance in parallel with a 19 nF capacitance of a piezoceramic shear patch, this means that the

oscilloscope reading can be considered *quite accurate*, whereas the acquisition board’s input impedance is too low and thus the measured voltage will be lower. This is the reason why we have measured the same voltage with the oscilloscope first and then, with the acquisition board; from these measurements we established *corrective factors* (1.95 for the free patch, 1.50 for the patch on the clamped side and 1.272 for the two patches parallel connection with inverse feedback). In other words, these coefficients allow us to include the corrective factor due to the lower impedance of the acquisition board. Besides, the oscilloscope cut-off frequency is 10 Hz; this means that at this frequency the corresponding measured signal is only 0.71 of its real value. Therefore, moving the working frequency to 24 Hz allows avoiding the potential influence of the AC coupling on the oscilloscope measurement.

The other test equipment used in the experiments is shown in Fig. 4(c); it consists of an Agilent wave generator type 33120A, a Bruël-Kjaër power amplifier type 2718 and a Bruël-Kjaër force transducer type 8230-001 (see Fig. 3). For the latter, 1 N corresponds to 22.48 mV.



(a) Acquisition board measurement-based experimental flowchart



(b) Digital oscilloscope measurement-based experimental flowchart

Fig. 5 Flowcharts of the performed dynamic sensing experiments on the smart sandwich plate benchmark

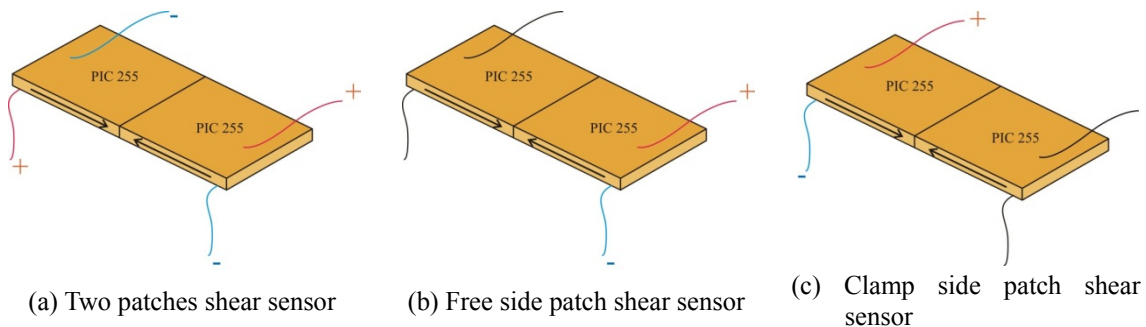


Fig. 6 The core patches electrical connections as (a) collective and (b)/(c) individual  $d_{15}$  shear sensor

Flowcharts of the performed dynamic  $d_{15}$  shear sensing experiments on the present cantilever smart sandwich benchmark are shown in Fig. 5. The first flowchart, Fig. 5(a), concerns the sensing experimental setup that uses the *acquisition board*, while the second one, Fig. 5(b), is related to the use of the *digital oscilloscope*. The associated *electrical connections* for the patches for the  $d_{15}$  shear sensing experiments are given in Fig. 6. In a first electrical configuration, as in Fig. 6(a), the two patches are connected in *parallel* with inverse feedback so that they sense *collectively* the produced response voltage, while in the second and third configurations, shown in Figs. 6(b) and 6(c) respectively, the right (at the plate tip) and left (near the plate clamp) patches sense *individually* the voltage in response to the applied harmonic (at 24 Hz) force. The measurements were conducted several times in order to check the repeatability of the experiments.

### 3.2 Experimental assessment

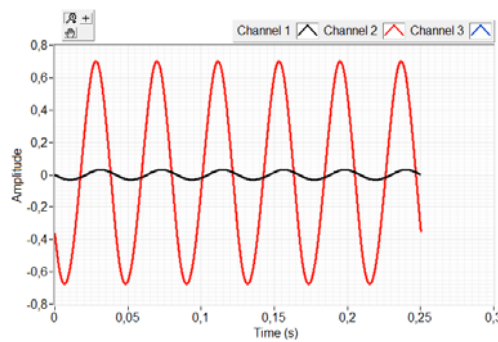
The *acquisition board* produced sensing *peak-to-peak* ( $V_{p-p}$ ) voltages under an applied harmonic (at 24 Hz) force of 2.8 N, corresponding to 62.99 mV of the force sensor, for the core sensor three electric connections as in Figs. 6 (a) - 6(c) are shown, respectively, in Figs. 7(a) - 7(c); each sensor voltage signal is shown together with that of the corresponding applied harmonic force. It can be noticed from Fig. 7 that the free side shear sensor, corresponding to the electric connection of Fig. 6(b), provides the highest sensing voltage amplitude; this can be seen better from the graphical superposition of the three sensing signals (from the three electric connections of Fig. 6) under the same amplitude applied force, as shown in Fig. 8. This qualitative sensing performance result is confirmed quantitatively by the three sensors produced maximum voltage *peak-to-peak* values, as given in Table 1. The latter shows that the clamp side patch has the smallest sensing capacity when it serves individually, while the parallel-connected patches sensing performance lies in between.

The sensed peak-to-peak voltages under harmonic (at 24 Hz) forces with different magnitudes, ranging from 0.35 to 2.8 N for the measurements using the acquisition board and ranging from 0.34 to 2.67 N for those using the oscilloscope, are illustrated in Figs. 9(a) and 9(b), respectively. The latter show a *linear* relationship between the sensed peak-to-peak voltages and the applied harmonic forces confirming the theoretical prediction of the section 2. They prove again the free-side patch performance superiority as individual shear sensor.

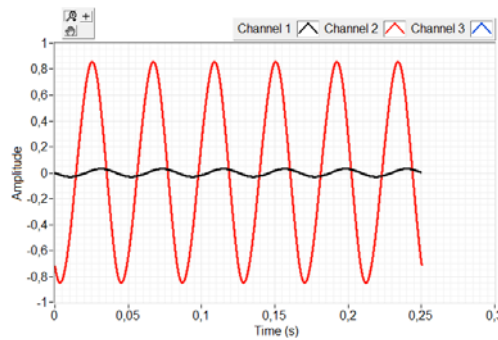
Table 2 presents the experimental sensed voltage to applied force ratios using the acquisition board and oscilloscope. It can be noticed that both measurement devices provide very close results. They also confirm the superiority of the free side patch as an individual shear sensor.

Table 1 Acquisition board sensed peak-to-peak voltages ( $V_{p-p}$ ) for the three sensor connections under an applied harmonic (at 24 Hz) force of 2.8 N

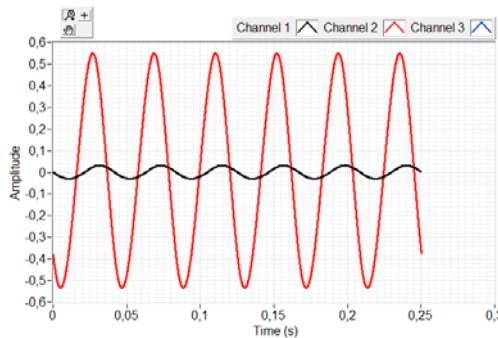
Patches electric connections	Sensed $V_{p-p}$ voltage (V)
Fig. 6(a): Two patches as collective sensor	1.376
Fig. 6(b): Free side patch as individual sensor	1.704
Fig. 6(c): Clamp side patch as individual sensor	1.084



(a) Two parallel-connected patches as in Fig. 6(a) and acting as a collective shear sensor



(b) Free side patch connected as in Fig. 6(b) and acting as an individual shear sensor



(c) Clamp side patch connected as in Fig. 6(c) and acting as an individual shear sensor

Fig. 7 Shear sensor peak-to-peak voltages (red curves, channel 2) and force (black curve, channel 1) versus time under a harmonic (at 24 Hz) force of 2.8 N

Table 2 Experimental sensed voltage/applied force ratios (V/N) from *acquisition board* and *oscilloscope*

Patches electric connections	Voltage/force ratio (V/N)	Voltage/force ratio (V/N)
	using <i>acquisition board</i>	using <i>oscilloscope</i>
Fig. 6(a): Two patches as collective sensor	0.4936	0.4959
Fig. 6(b): Free side patch as individual sensor	0.6092	0.6152
Fig. 6(c): Clamp side patch as individual sensor	0.3887	0.3900

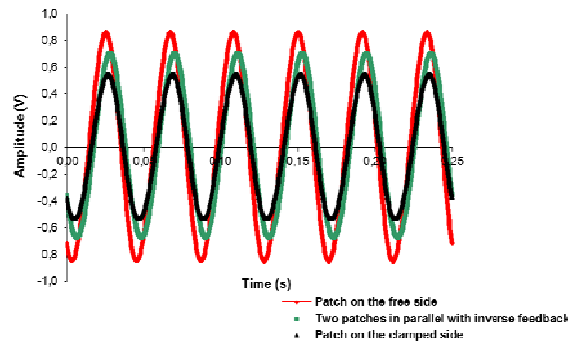
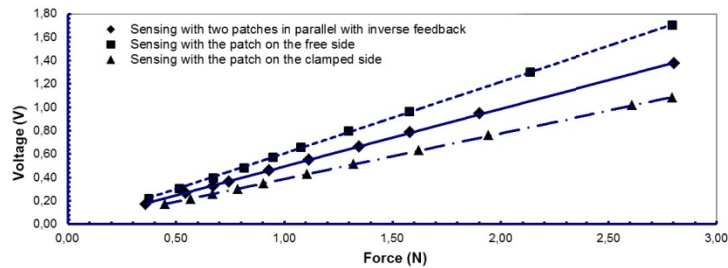
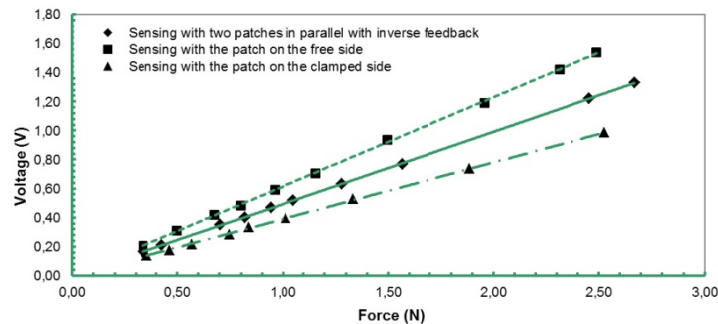


Fig. 8 Superposed produced *peak-to-peak* voltages by the three sensors configurations of Figs. 6(a) - 6(c) under the same harmonic (at 24 Hz) force amplitude of 2.8 N



(a) *Acquisition board* generated sensed peak-to-peak voltages vs. applied harmonic force amplitudes



(b) *Oscilloscope* generated sensed peak-to-peak voltages vs. applied harmonic force amplitudes

Fig. 9 Experimental sensed peak-to-peak voltages vs. applied harmonic forces for the three sensor connections

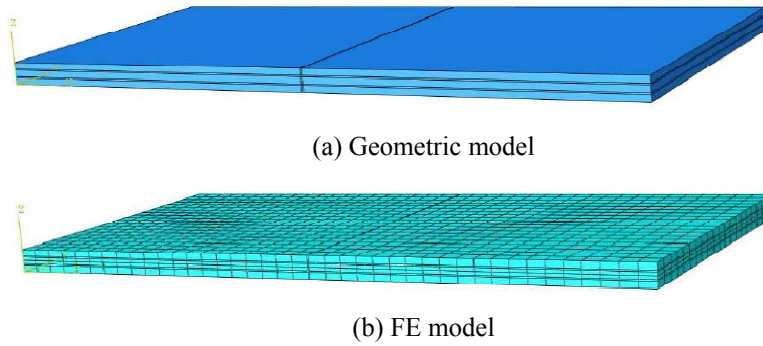


Fig. 10 The smart sandwich plate (a) geometric and (b) FE models

### 3.3 Numerical verifications

For the verification of the experimental dynamic sensing results, the  $d_{15}$  shear piezoelectric smart sandwich plate benchmark was simulated using ABAQUS<sup>®</sup> 3D piezoelectric coupled FE. Hence, within the latter, the dynamic implicit analysis option was retained by applying periodic (at 24 Hz) force amplitudes and supplying a slight damping, through the time integrator factor ( $\alpha=-0.05$ ), to the dynamic time integration scheme. Piezoelectric (C3D20E) and elastic (C3D20) quadratic (20 nodes) brick elements are used for the piezoceramic patches, GFRP composite faces and interface adhesive layers. The in-ward OP polarization orientation is implemented by changing the sign of the patches individual piezoelectric matrices. Assuming a thickness of 0.1 mm for the core-to-faces interfaces and vertical inter-patches adhesive layers, the benchmark geometric model is shown in Fig. 10(a). The corresponding FE mesh is shown in Fig. 10(b); it has 2 elements through the shear piezoceramic core thickness and 1 element through each of the GFRP and adhesive layers thickness. Besides, the piezoceramic, GFRP and adhesive layers were divided into 40 elements along their length and 20 elements along their width, leading to a FE model of 33062 nodes and 4800 elements. The materials properties used in the simulations are given in the Appendix.

The FE model was mechanically updated (MU) by softening the theoretically perfect (hard) clamp (nil mechanical displacements) boundary conditions (BC). Therefore, the three nil translations along the 3D coordinate system axes were dropped to the benefit of blocking only the two translations in the cross-section plane; besides, the translation along the plate first ( $x$ ) axis was left free but linked to linear springs which stiffness is distributed on all the face nodes, as in Fig. 11(a), using the software *Spring/Dashpots* function. This modification allows the first (clamped) section to rotate around the  $y$ -axis so that the clamp becomes less stiff.

Different spring stiffness values per node  $k$  were tested using the classical trial and error technique, but within an error optimization and minimization procedure that uses this measure

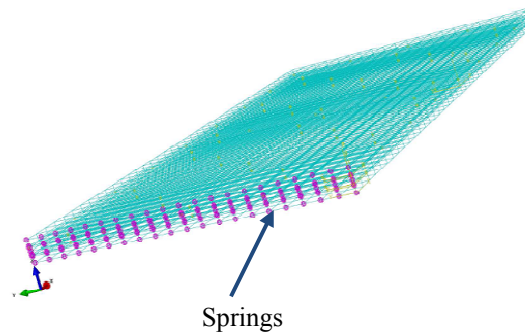
$$e^2 = [V_1 - \bar{V}_1(k)]^2 + [V_2 - \bar{V}_2(k)]^2 + [V_3 - \bar{V}_3(k)]^2 \tag{18}$$

where  $V_1$ ,  $\bar{V}_1(k)$ ,  $V_2$ ,  $\bar{V}_2(k)$ ,  $V_3$ , and  $\bar{V}_3(k)$  are, respectively, the maximum produced voltage values by the free side patch experimentally, by the free side patch in the FE simulation after MU

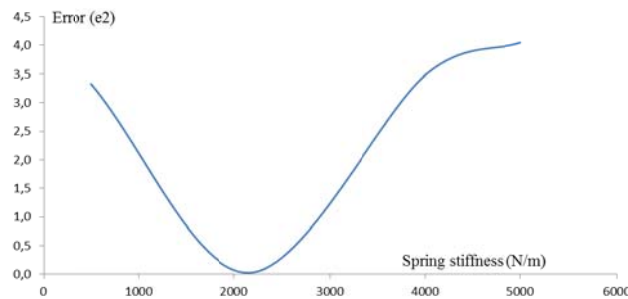
with the nodal spring stiffness  $k$ , by the clamp side patch experimentally, by the clamp side patch in the FE simulation after MU with the nodal spring stiffness  $k$ , by the parallel with inverse feedback connection of the two patches experimentally, and by the parallel with inverse feedback connection of the two patches in the FE simulation after MU with the nodal spring stiffness  $k$ .

As can be seen from the graphical representation of the error measure, as defined in Eq. (18), in Fig. 11(b), the nodal spring stiffness value of 2.16 kN/m gives the minimal error ( $e^2$ ) value of 0.028 which corresponds to a very good correlation between the performed tests and their FE simulations.

The electrodes potential distributions (EPOT) of the clamp side (blue) and free side (red) patches before and after MU under an harmonic (at 24 Hz) force of 2.8 N are shown in Fig. 12. It is worth to stress that these results represent the maximum generated voltage values; they correspond to the maximum produced *peak-to-peak* voltage ( $V_{p-p}$ ) values in the experiments. By analyzing their color legend EPOT values, these figures show that the influence of the clamp on the electrode potential of its adjacent patch is not ignorable. Hence, the sensing ability of the patch adjacent to the clamp is enormously affected by the stiffness of the clamp which is much softer in reality (experiments) than in the ideal situation (non MU FE simulations). Nevertheless, for the parallel with inverse feedback connection, there is a moderate influence of the clamp; this is due to the fact that the corresponding shown EPOT represents the mean electrode potential distribution value of the adjacent and free-side patches. Also, the sensed voltage of the clamp side patch was smaller than the free side one. From all these results, it can then be concluded that the MU is necessary for realistic sensing simulations.



(a) Integrated nodal springs at the cantilevered side of the plate



(b) Error ( $e^2$ ) versus nodal spring stiffness (N/m)

Fig. 11 Mechanical updating of the smart sandwich plate FE model

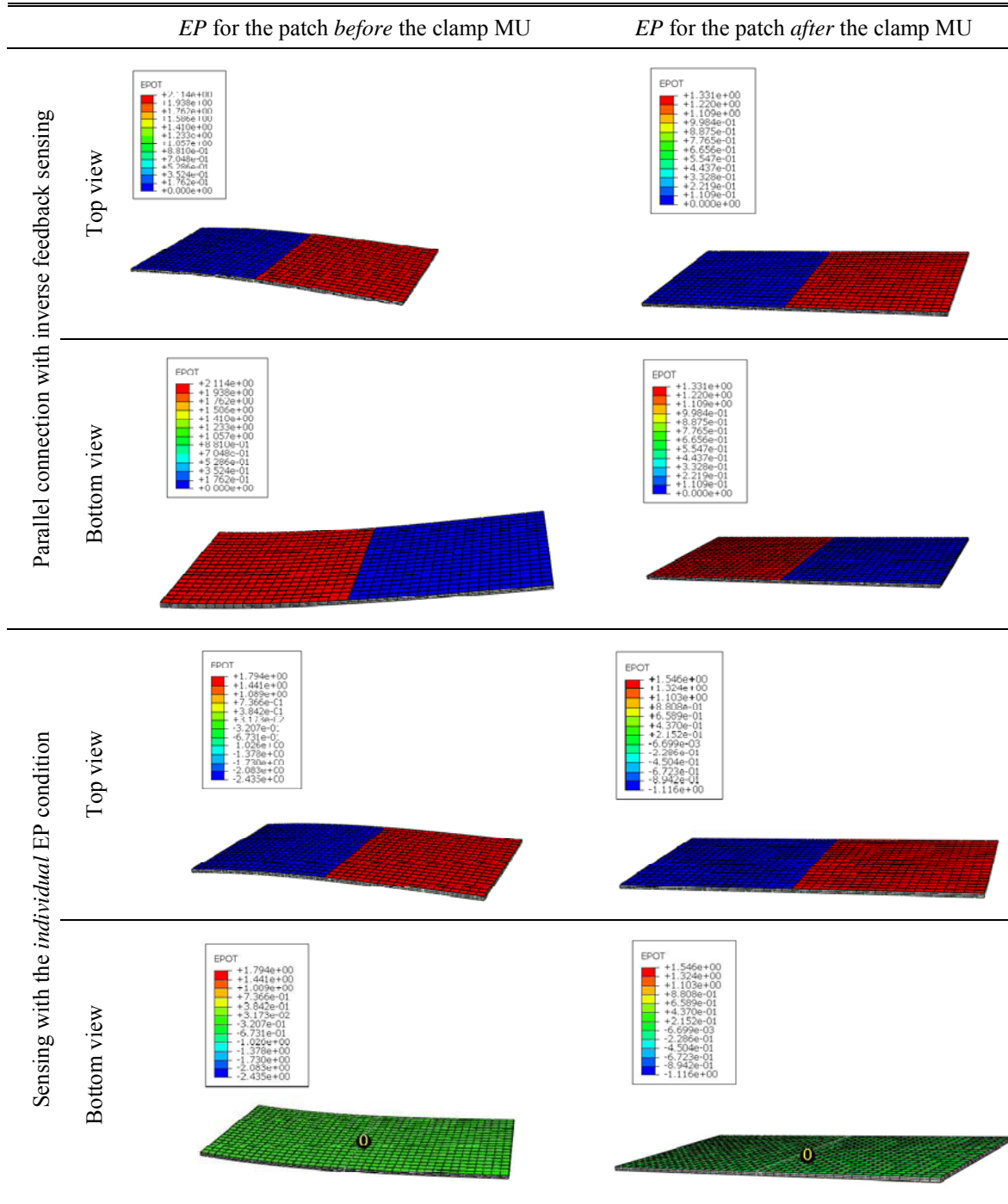
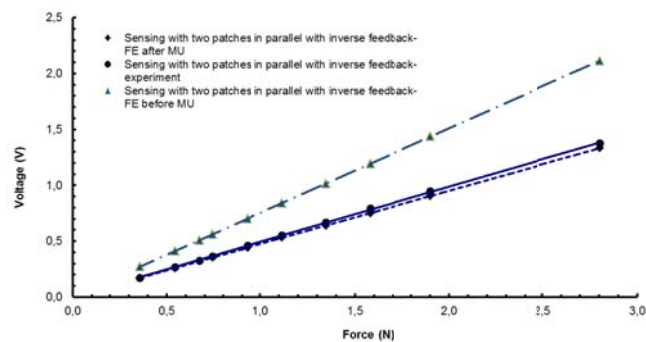
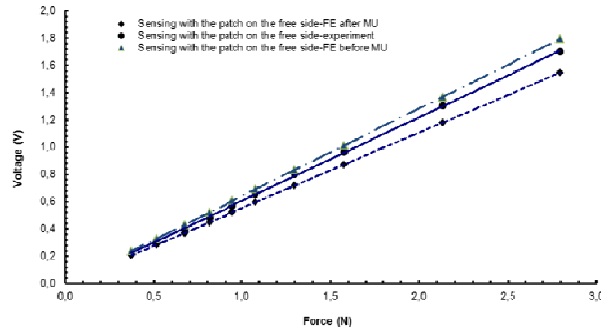


Fig. 12 Electrodes potential distributions under harmonic (at 24 Hz) force of magnitude 2.8 N

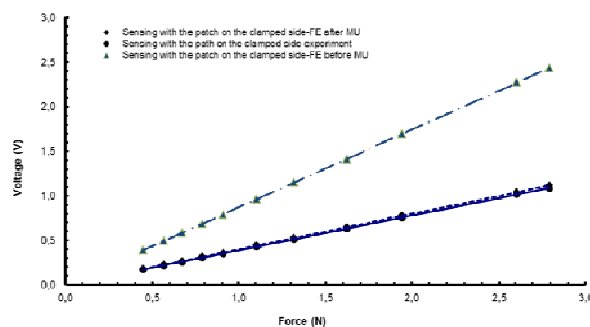
Using the graphically optimized spring stiffness value of 2.16 kN/m in the clamp MU of the FE model of the cantilever shear piezoelectric smart plate benchmark led to the quantitative simulation results and test (*acquisition board*)/model relative deviations summarized in Table 3. The latter shows a good test/model correlation for the patch on the free side even before the MU; this can be explained by the fact that it is not much affected by the clamp. Yet, the parallel-connected two patches and, particularly, the patch adjacent to the clamp require the MU in order to reach an acceptable test/model correlation. As stated above, this is due to the fact that the real (experimental) clamp is much softer than the ideally considered one in the corresponding FE simulation models.



(a) Sensing with *parallel-connected patches* with inverse feedback



(b) Sensing with the *free side* patch



(c) Sensing with the *clamp side* patch

Fig. 13 Maximum generated *peak-to-peak* voltages under harmonic (at 24 Hz) force of *varied* magnitude

Under varied amplitudes of the applied harmonic (at 24 Hz) force, the 3D FE simulation results for the maximum generated *peak-to-peak* voltages, before and after the clamp MU, are compared to the experimental ones in Fig. 13 for the piezoceramic  $d_{15}$  shear core sensor three electric connections. It can be particularly observed that the free side patch sensor is the less affected by the clamp realization and simulation (even before the MU). The numerical-to-experimental results comparison confirms the superior performance of the free side patch as an individual  $d_{15}$  shear sensor; it is then recommended to choose a tip position of the patch sensor for a mechanical cantilever configuration.

Table 3 Maximum generated *peak-to-peak* voltages under a harmonic (at 24 Hz) force of magnitude 2.8 N

Generated peak-to-peak voltage (V) Patches electric connections	Exp.	Numerically via FE simulation			
		Before MU	Err* (%)	After MU	Err* (%)
Fig. 6(a): <i>Two patches as collective sensor</i>	1.376	2.114	53.63	1.331	-3.27
Fig. 6(b): <i>Free side patch as individual sensor</i>	1.704	1.794	5.28	1.546	-9.27
Fig. 6(c): <i>Clamp side patch as individual sensor</i>	-1.084	-2.435	124.63	-1.116	2.95

#### 4. Conclusions

In this work, an axially in-ward oppositely poled piezoceramic  $d_{15}$  shear two-patches core, sandwiched between two glass fiber reinforced polymer composite faces, of a cantilever smart sandwich plate has been assessed with the two patches acting as a collective or an individual sensor under an applied harmonic (at 24 Hz) force of varying amplitude. The maximum sensed *peak-to-peak* voltages have been measured by an acquisition board and a digital oscilloscope. It has been observed experimentally that (i) the free side patch has the highest capability to serve as an individual sensor, (ii) the clamp side patch appears less efficient, and (iii) the parallel with inverse feedback connected two patches have a performance in between the previous two electrical connections. The experimental results were then compared to their 3D finite element simulations; the latter considered realistic simulation features like electrodes equipotential condition and the clamp mechanical updating. It has been found in particular that the clamp stiffness, which is much softer than its ideal model, has an enormous influence on the sensed voltage of its adjacent patch; therefore shear sensing with a free side patch would be advantageous for a cantilever configuration.

#### Acknowledgments

This work has been supported by the Linz Center of Mechatronics (LCM) in the framework of the Austrian COMET-K2 programme. The authors would like also to thank the technical assistance of Dr. A. Kosecki during the tests at the Institut Supérieur de Mécanique de Paris.

## References

- Benjeddou, A. (2007), "Shear-mode piezoceramic advanced materials and structures: a state of the art", *Mech. Adv. Mater. Struct.*, **14**(4), 263-275.
- Benjeddou, A., Poizat, C. and Gall, M. (2006), "First use of the shear actuation mechanism for valve-less piezoelectric micro-pump design", *Proceedings of the 8<sup>th</sup> International Conference on Computational Structures Technology*, Las Palmas de Gran Canaria, Spain.
- Berik, P. and Benjeddou, A. (2011), "Static experimentations of the piezoceramic  $d_{15}$ -shear actuation mechanism for sandwich structures with opposite or same poled patches-assembled core and composite faces", *Int. J. Smart Nano Mater.*, **2**(4), 230-244.
- Berik, P., Benjeddou, A. and Krommer, M. (2013), "Piezoceramic  $d_{15}$  shear-induced direct torsion actuation mechanism: a new representative experimental benchmark", *Smart Struct. Syst.*, **12** (5), 483-499.
- Cheng, C.H., Chen, S.C., Kuo, H.C. and Chou, Z.B. (2005), "The poling design of a shear mode piezoelectric actuator", *J. Micromech. Microeng.*, **15**, 2163-2171.
- Chevallier, G., Berik, P., Benjeddou, A. and Krommer, M. (2013), "Experimental static response characteristics of piezoceramic  $d_{15}$  shear-induced torsion sensing and actuation mechanisms", *Sens. Actuat. A-Phys.*, submitted.
- Han, R. and Shi, Z. (2012), "Dynamic analysis of sandwich cement-based piezoelectric composites", *Compos. Sci. Technol.*, **72**, 894-901.
- Konca, H.P. and Wahab, M.A. (2012), "The effects of embedded piezoelectric fiber composite sensors on the structural integrity of glass fiber epoxy composite laminate", *Smart Mater. Struct.*, **21**, 015016 (9pp).
- Kursu, O., Kruusing, A., Pudas, M. and Rahkonen, T. (2009), "Piezoelectric bimorph charge mode sensor", *Sens. Actuat. A - Phys.*, **153**, 42-49.
- Melnikowskycz and Brunner, A.J. (2011), "The performance of integrated active fiber composites in carbon fiber laminates", *Smart Mater. Struct.*, **20**, 075007 (8pp).
- Ma, L., Melkote, S.N., Morehouse, J.B., Castle, J.B., Fonda, J.W. and Johnson, M.A. (2012), "Design of thin-film polyvinylidene fluoride sensor rosettes for isolation of various strain components", *J. Intell. Mater. Syst. Struct.*, **23**(10), 1119-1130.
- Rausch, J., Hatzfeld, C., Karsten, R. and Kraus, R. (2012), "Strain measurement on stiff structures: experimental evaluation of three integrated measurement principles", *Smart Mater. Struct.*, **21**(6), 064008 (9pp).
- Sung, C.C., Varadan, V.V., Bao, X.Q. and Varadan, V.K. (1994), "Active torsion vibration control experiments using shear-type piezoceramic sensors and actuators", *J. Intell. Mater. Syst. Struct.*, **5**, 436-442.
- Van Den Ende, D.A., Groen, W.A. and Van Der Zwaag, S. (2010) "Development of temperature stable charge based piezoelectric composite quasi-static sensors", *Sens. Actuat. A - Phys.*, **163**, 23-31.
- Wang, D.A. and Liu, N.Z. (2011), "A shear mode piezoelectric harvester based on a pressurized water flow", *Sens. Actuat. A - Phys.*, **167**(2), 449-458.

### Appendix

The smart sandwich structures piezoceramic core and composite faces materials properties are recalled from Berik and Benjeddou (2011), together with the adhesive material data, in Table 4. Note that for activating the  $d_{15}$  shear sensing mechanism using these PIC255 PZT data, the *axially poled* piezoceramic patches should have their material axis 1 (poling direction) lying geometrically along the global  $x$ -axis of the structure.

Table 4 Materials properties of the sandwich structures core PZT PIC255 patches, glass fiber/epoxy composite faces, adhesive glue

Materials	Constants	Notations	Values
PIC255 (PI Germany) Poled along $x$ -axis	Piezoelectric coupling	$e_{15}=e_{24}$	11.9
	<i>stress</i> constants ( $C/m^2$ )	$e_{31}=e_{32}$	-7.15
		$e_{33}$	13.7
	Dielectric constants at constant <i>strain</i> (nF/m)	$\epsilon_{22}^s=\epsilon_{33}^s$	8.234
		$\epsilon_{11}^s$	7.588
	Young's moduli ( $GN/m^2$ )	$E_2=E_3$	62.89
		$E_1$	47.69
	Shear moduli ( $GN/m^2$ )	$G_{13}=G_{12}$	22.26
		$G_{23}$	23.15
	Poisson's ratios	$\nu_{13}=\nu_{12}$	0.46
$\nu_{23}$		0.36	
Mass density ( $kg/m^3$ )	$\rho$	7800	
Glass fiber/epoxy (Hexcel Austria)	Young's moduli ( $GN/m^2$ )	$E_2=E_3$	13.1
		$E_1$	33.11
	Shear Moduli ( $GN/m^2$ )	$G_{13}=G_{12}$	3
		$G_{23}$	2.3
	Poisson's ratios	$\nu_{13}=\nu_{12}$	0.27
		$\nu_{23}$	0.4
Mass density ( $kg/m^3$ )	$\rho$	2620	
Adhesive glue (Henkel Loctite 9466)	Young's moduli ( $GN/m^2$ )	$E$	1.718
	Poisson's ratio	$\nu$	0.36
	Mass density ( $kg/m^3$ )	$\rho$	1000